

Research article

Adaptive photoacoustic computed tomography

Manxiu Cui ^a, Hongzhi Zuo ^a, Xuanhao Wang ^a, Kexin Deng ^b, Jianwen Luo ^b, Cheng Ma ^{a,*}^a Department of Electronic Engineering, Tsinghua University, Beijing, 100084, China^b Department of Biomedical Engineering, School of Medicine, Tsinghua University, Beijing, 100084, China

ARTICLE INFO

Keywords:

Photoacoustic computed tomography
Ring array
Image reconstruction
Speed of sound
Adaptive optics
Phase diversity

ABSTRACT

For many optical imaging modalities, image qualities are inevitably degraded by wavefront distortions caused by varying light speed. In optical microscopy and astronomy, adaptive optics (AO) has long been applied to compensate for such unwanted aberrations. Photoacoustic computed tomography (PACT), despite relying on the ultrasonic wave for image formation, suffers from the acoustic version of the same problem. However, this problem has traditionally been regarded as an inverse problem of jointly reconstructing both the initial pressure and the sound speed distributions. In this work, we proposed a method similar to indirect wavefront sensing in AO. We argued that wavefront distortions can be extracted and corrected by a frequency domain analysis of local images. In addition to an adaptively reconstructed aberration-free image, the speed of sound map can be subsequently estimated. We demonstrated the method by *in silico*, phantom, and *in vivo* experiments.

1. Introduction

The photoacoustic (PA; or optoacoustic, OA) effect refers to the process of converting light absorption into ultrasound emission. It offers a unique way of measuring optical absorption by ultrasonic detection [1]. Photoacoustic computed tomography (PACT), which employs spatially distributed detection of PA signals and digital image reconstruction, allows tomograms of light absorption to be formed in the optically diffusive regime with relatively high resolution [2].

During PA image reconstruction, the commonly assumed constant speed of sound (SOS) is only an approximation, which generates image artifacts in the presence of acoustic heterogeneity. If the SOS distribution is measured to assist image reconstruction, the image quality can be greatly improved [3–6]. However, the measurement of the SOS requires additional hardware with increased system complexity and cost. Alternatively, it is more desirable to perform joint reconstruction (JR) of the SOS and the PA initial pressure (IP), based upon PA signals alone [7–17]. To do so, the frequency domain [8–10] or time domain [11–13] model-based reconstructions incorporating the acoustic wave equation in heterogeneous media can be adopted. The solution is usually found by iterative optimization to minimize the difference between the measured signals and the predicted ones. Back-projection based JR techniques count on the correlation between images reconstructed using partial data (e.g. two half-ring reconstructions [14], first and second half-time

reconstructions [15]) to search for the correct SOS distribution. However, mathematically, JR of the SOS and the IP is fundamentally unstable and the uniqueness of the solution is only guaranteed in some special cases [18–20]. Numerical studies also found that the optimization process in the JR problem is not convex [12], which means that the solution can easily fall into local extrema.

Non-uniform SOS causes wavefront distortions, which ultimately give rise to resolution reduction and image artifacts. Here, comparing the wavefront distortions caused by spatially varying wave speed in PACT with that in light microscopy is enlightening. As shown in Fig. 1, central to the image formation of light microscopy and PACT is a mapping (i.e., ideally representing an identity matrix) from the object domain to the image domain. In optical microscopy, such a mapping is simply done by physical lenses, while in PACT, the mapping is accomplished digitally by reversing the recorded PA waveforms. Fig. 1(b) depicts the imaging process of a standard PACT system based on a ring array [21]. In this case, ultrasound detection is focused in the elevational direction, allowing thin slices of the object to be imaged in 2D (i.e., sectioning). To refocus an image, the back-projection image reconstruction algorithm [22] is commonly used, which can be interpreted as triangulation localization [23]. Specifically, the PA signals are back-projected to arcs that are centered at the positions of the transducer elements. In particular, to image a point source, the radii of the arcs are determined by timing the PA waveforms and assuming a constant speed

* Corresponding author.

E-mail addresses: mccui@caltech.edu (M. Cui), zuohz19@mails.tsinghua.edu.cn (H. Zuo), xh-wang17@mails.tsinghua.edu.cn (X. Wang), dkx17@mails.tsinghua.edu.cn (K. Deng), luo_jianwen@tsinghua.edu.cn (J. Luo), cheng_ma@tsinghua.edu.cn (C. Ma).

of sound. Ideally, the arcs are expected to intercept and constructively interfere at the source point to form a bright spot.

In fluorescence microscopy, the optical wavefront from a fluorescent point source is often distorted by the spatially varying refractive index of the biological sample, as shown in Fig. 1(a) [24]. The light rays, as depicted by the green lines, fail to converge to the same point on the image plane, resulting in degraded resolutions. In PACT, how the unknown SOS distribution produces wavefront aberration can be understood similarly. As shown in Fig. 1(b), if the acoustic refractive index, i.e. the SOS, is non-uniform, the PA wavefront from a point source will be distorted and eventually back-projected into an irregular pattern [25]. As a result, the reconstructed image features will be distorted and/or split.

The wavefront distortions in optical microscopy can be measured, either directly [26–33] by a Shack-Hartmann wavefront sensor or indirectly [34–41] and subsequently compensated for by a spatial light modulator or a deformable mirror. Known as adaptive optics (AO), this technology was first implemented in astronomic telescopes and then successfully translated into microscopy [42]. In terms of wavefront distortion caused by unknown SOS distribution, the similarity between optical microscopy and PACT suggests that the concept of AO can be extended beyond purely optical imaging. In this paper, we implemented a technique that can solve the JR problem analogous to indirect wavefront measurement in conventional AO: The image is reconstructed patch by patch; within each patch, the wavefront distortion is almost identical (i.e., an “isoplanatic patch”) and can be extracted from the local point spread function (PSF). The advantage of indirect AO is that it does not need a point target to be created as a real “guide star”, while seeks to optimize the compensation wavefront from a number of images at the cost of increased total exposure times [43]. In our method, the PACT image series can be generated digitally rather than physically, and our wavefront extraction is similar to the “phase diversity” method [44]. The local PSF, which has long been regarded as an unknown, can be computationally found from a stack of local images reconstructed with different delays. Thereby, the full image can be better focused via piecewise deconvolution. As a bonus, once the wavefronts of all the patches are determined, they can be used collectively to compute the

global SOS map. Unlike all JR approaches which tend to be corrupted by incorrect guess of the SOS distribution, our method bypasses the cumbersome global searching of the SOS map, thus improves the stability and reliability of the solution. To acknowledge the key role played by the concept of AO, we named this technique Adaptive PACT (APACT) and demonstrated *in silico*, phantom, and *in vivo* experiments.

2. Method

2.1. Wavefront function and point spread function

In the focused ring array PACT system, 512 transducer elements are evenly arranged on a circle with a diameter of 10 cm. A detailed description of the system and its operating process can be found in [14].

In a homogenous medium with a constant SOS of \hat{v}_s , the universal back-projection formula [22] directly links $P_0(\mathbf{r}')$, the IP at time zero when the optical energy is absorbed, to $p(\mathbf{r}, t)$, the pressure on a surface that encloses the sources:

$$P_0(\mathbf{r}') = p(\mathbf{r}', 0) = \int_{\Omega_0} (2p(\mathbf{r}, t) - 2t \frac{\partial p(\mathbf{r}, t)}{\partial t}) \Big|_{t=\frac{\|\mathbf{r}'-\mathbf{r}(n)\|}{\hat{v}_s}} d\Omega_0 / \Omega_0. \quad (1)$$

where $d\Omega_0$ is the solid angle subtended by a transducer element at \mathbf{r} from the source point at \mathbf{r}' . In real practice, the second term on the right is often dominant [22]. The above formula assumes the detectors have infinite bandwidth, uniform angular response, and be distributed over 4π solid angle. In reality, the transducers are band limited and their angular responses are not flat. Also, the array is focused in the elevational direction, converting the reconstruction from 3D to 2D. Due to these limitations, we implemented the following delay and sum (DAS) algorithm instead of Eq. (1) in practice:

$$I(\mathbf{r}') = \sum_{n=1}^N S(n, t) \Big|_{t=\frac{\|\mathbf{r}'-\mathbf{r}(n)\|}{\hat{v}_s}}, \quad (2)$$

where $\mathbf{r}(n)$ and $S(n, t)$ are the location (in 2D) and the output of the n 'th transducer, respectively. N is the total number of transducers. $I(\mathbf{r}')$ is the

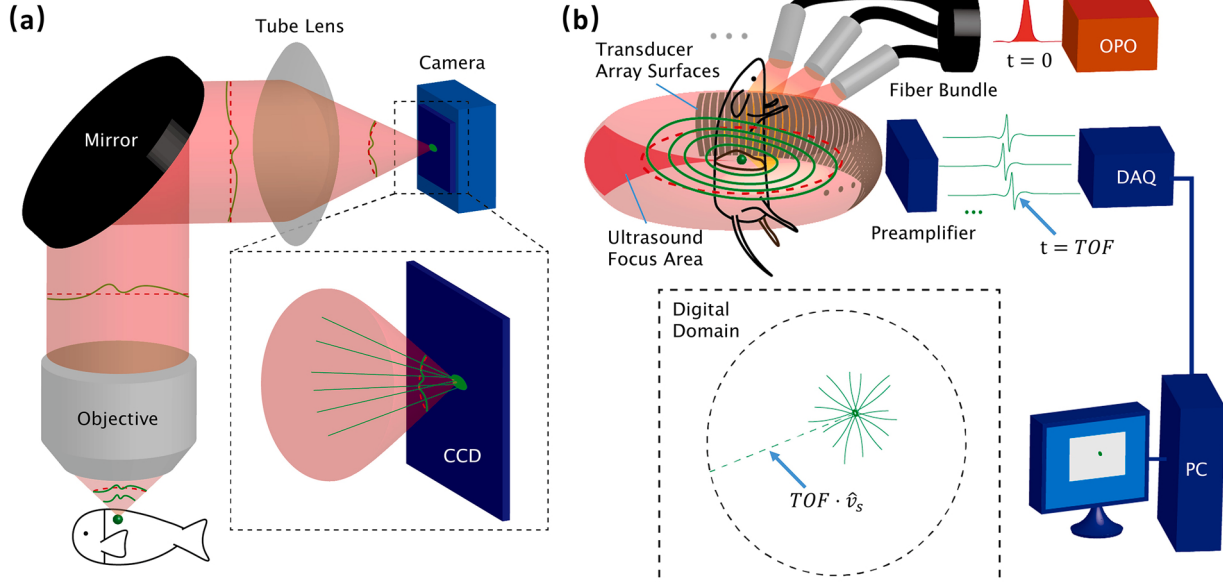


Fig. 1. Comparison between optical microscopy and PACT systems. Both imaging processes are affected by wavefront distortion. (a) A wide-field fluorescence microscope. The red dashed lines are the ideal distortion-free wavefronts and the green lines are the distorted wavefronts and light rays. (b) A PACT imaging system. The red dashed circle is the ideal distortion-free photoacoustic wavefront. The green curves are distorted wavefronts. In the digital domain, the green arcs are the back-projection curves in the PACT reconstruction algorithm. (For interpretation of the references to colour in this figure legend, the reader is referred to the web version of this article).

reconstructed image, which is an approximation to $P_0(\mathbf{r}')$. In real practice, Eq. (2) is a reasonable approximation to the back-projection formula, because the response of our transducer can be roughly treated as a time derivative. In addition, although the method described in this paper is based on DAS, it can be applied to the back-projection formula (Eq. (1)) in which additional linear filtering is performed on $S(n, t)$.

Now, we consider a point source located at \mathbf{r}' and analysis its image. The back-projection arcs, mathematically described by $t = \frac{\|\mathbf{r}' - \mathbf{r}(n)\|}{\hat{v}_s}$, will intercept at \mathbf{r}' only if the real time of flight (TOF) of the PA signal coincides with that of a perfect spherical wavefront propagating at \hat{v}_s . We define any deviation from the above ideal case as the wavefront function:

$$w(\theta, \mathbf{r}') = \|\mathbf{r}' - \mathbf{r}\| - TOF(\mathbf{r}', \mathbf{r})\hat{v}_s. \quad (3)$$

Here θ denotes the angle of a vector pointing from \mathbf{r} to \mathbf{r}' , and $TOF(\mathbf{r}', \mathbf{r})$ is the ultrasound propagation time from \mathbf{r}' to \mathbf{r} .

By adding up all the back projection arcs, the image of a point source with unit amplitude (the point spread function, PSF) is obtained, mathematically expressed as $PSF(\mathbf{x}; w(\theta, \mathbf{r}'))$. In the DAS algorithm, the back projection arcs are broadened into thin bands whose cross-sectional profiles are determined by the electrical impulse response

(EIR) of the transducers $h(t)$. It can be shown that the PSF is mathematically determined by the wavefront function (see Appendix A for further details):

$$PSF(\mathbf{x}; w(\theta, \mathbf{r}')) = \sum_{i=1}^N \frac{A}{\|\mathbf{r}' - \mathbf{r}(i)\|} h\left(\frac{\hat{n}_i \cdot \mathbf{x} + w(\theta_i, \mathbf{r}')}{\hat{v}_s}\right) \quad (4)$$

Here A is a constant and \mathbf{x} denotes the position in a shifted coordinate system whose origin coincides with \mathbf{r}' . The unit vector $\hat{n}_i = \frac{\mathbf{r}' - \mathbf{r}(i)}{\|\mathbf{r}' - \mathbf{r}(i)\|}$ whose polar angle is θ_i , represents the backpropagation direction. As in AO microscopy, the wavefront function changes with \mathbf{r}' . However, it is reasonable to treat $w(\theta)$ to be unchanged inside the isoplanatic patch. Under this assumption, the PSF becomes space-invariant, and thus the local image can be expressed as a convolution:

$$I(\mathbf{r}') = P_0(\mathbf{r}') * PSF(\mathbf{r}'; w(\theta)) \quad (5)$$

2.2. Wavefront extraction and adaptive reconstruction algorithm

Fig. 2 illustrates the working principle of the algorithm using simulation data, where the red box in **Fig. 2(a)** depicts one representative isoplanatic patch. The algorithm starts by adding a varying delay during the DAS process, resulting in

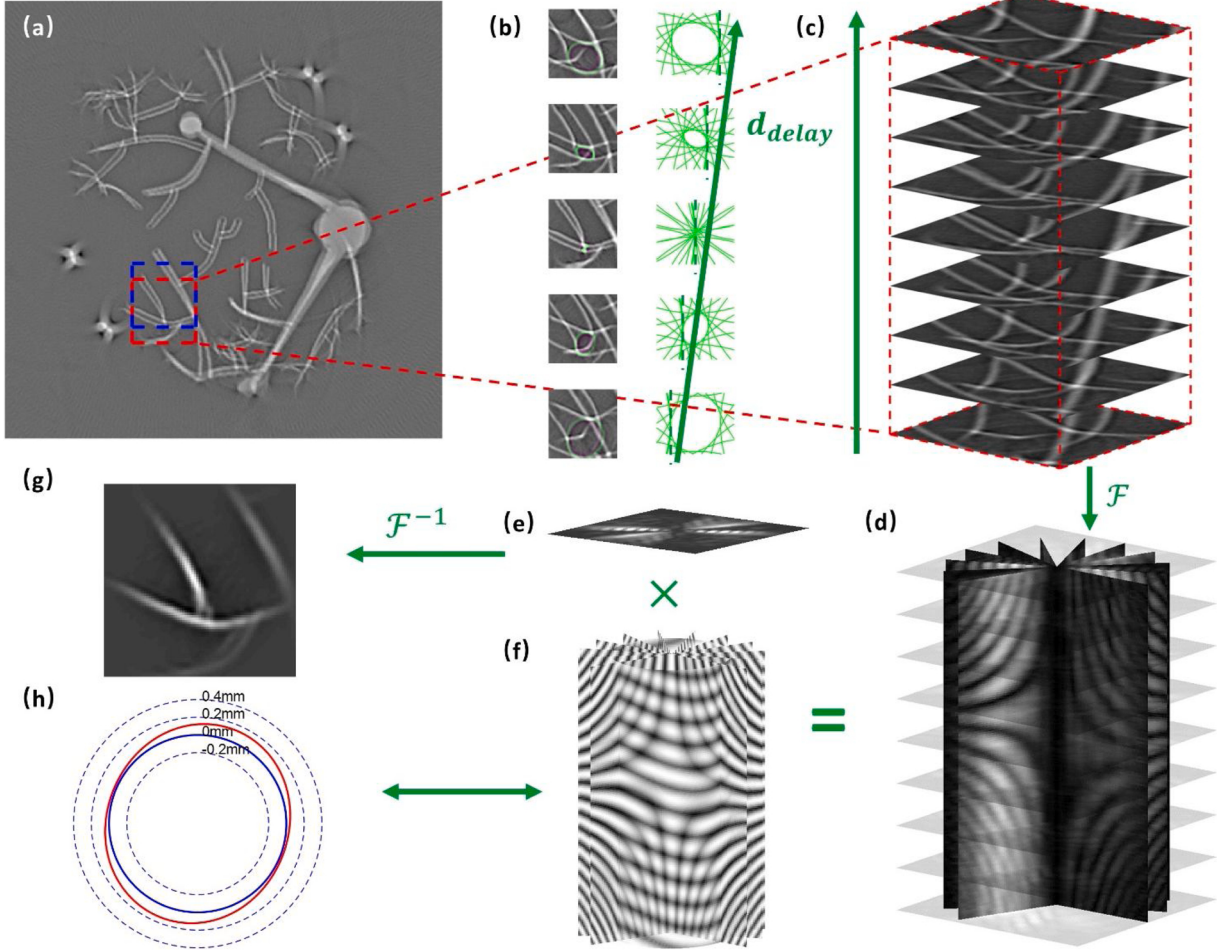


Fig. 2. Diagram of the APACT algorithm. All images are obtained from numerical simulation. (a) Image reconstructed with conventional DAS. The red box is one isoplanatic patch and the blue box is the successive one. (b) Left column: a stack of images reconstructed with increasing d_{delay} ; In each plot, the outline of a point spread function is highlighted in green. Right column: in each plot 16 back-projection arcs are shown to explain how the PSF is formed. The curvatures of the arcs are exaggerated. (c) A 3D rendering of the data cube $I(\mathbf{r}', d_{delay})$. (d) The Fourier transform of the images $F(\mathbf{k}, d_{delay})$ stacked together as in (c) with several radial slices. (e) The Fourier transform of the aberration-free image $\hat{F}(\mathbf{k})$. (f) The transfer function $TF(\mathbf{k}, d_{delay}; w(\theta))$ in which we also provide some slices to show the pattern. (g) The recovered aberration-free image $\hat{I}(\mathbf{r}')$. (h) The extracted wavefront function $w(\theta)$. (For interpretation of the references to colour in this figure legend, the reader is referred to the web version of this article).

$$I(\mathbf{r}', d_{\text{delay}}) = \sum_{n=1}^N S(n, t) \Big|_{t=\frac{\|\mathbf{r}' - \mathbf{r}(n)\| - d_{\text{delay}}}{v_s}}, \quad (6)$$

where d_{delay} is the extra delay distance and $I(\mathbf{r}', d_{\text{delay}})$ is the corresponding image of the isoplanatic patch reconstructed by DAS. By doing so, the radii of the back-projection arcs vary by the same amount of d_{delay} and the PSF becomes $\text{PSF}(\mathbf{r}'; w(\theta) - d_{\text{delay}})$. It should be noted that similar operations are common in conventional DAS when \hat{v}_s is adjusted [45] to better focus an image. This can be regarded as the 0th order compensation, and the process is illustrated in Fig. 2(b).

Now we prove that from a series of images $I(\mathbf{r}', d_{\text{delay}})$ ($d_{\text{delay}} = d_0, d_1, d_2, \dots$), we are ready to extract the wavefront function $w(\theta)$ as well as the aberration-free image $\hat{I}(\mathbf{r}')$, whose PSF corresponds to vanished wavefront aberration: $\text{PSF}(\mathbf{r}'; 0)$. This technique is similar to the phase diversity [44] method in optics. Note that when d_{delay} is varied, the local image $I(\mathbf{r}', d_{\text{delay}})$ will change accordingly. This is because $I(\mathbf{r}', d_{\text{delay}})$ is generated by convolving the initial pressure $P_0(\mathbf{r}')$ with a PSF whose shape is determined by $w(\theta)$ and d_{delay} . So $w(\theta)$ is encoded in the datacube $I(\mathbf{r}', d_{\text{delay}})$ (the third dimension is d_{delay}). In our study, we scanned d_{delay} in 161 discrete steps. The interval was 10 μm. In Eq. (6) we can see that this interval is small enough for the 40 MHz sampling rate. The maximum length of d_{delay} (both negative and positive value) is chosen to be a quarter of the edge length of the isoplanatic patch. This can guarantee that the defocused local image features are mostly confined within the patch as shown in Fig. 2 (b), which means the back-projection curves do not completely move out of the patch window. To extract the information concealed by the convolution operation, we turn to the spatial frequency domain as shown in Fig. 2(c) and (d). By doing so, convolution is converted to multiplication, and the effect of wavefront distortion is readily modeled by a multiplicative transfer function TF :

$$\begin{aligned} F(\mathbf{k}, d_{\text{delay}}) &= \mathcal{F}\{I(\mathbf{r}', d_{\text{delay}})\} \\ &= \mathcal{F}\{P_0(\mathbf{r}') * \text{PSF}(\mathbf{r}', w(\theta) - d_{\text{delay}})\} \\ &= \mathcal{F}\{P_0(\mathbf{r}') * \text{PSF}(\mathbf{r}', 0)\} \text{TF}(\mathbf{k}, d_{\text{delay}}; w(\theta)) \\ &= \mathcal{F}\{\hat{I}(\mathbf{r}')\} \text{TF}(\mathbf{k}, d_{\text{delay}}; w(\theta)) \\ &= \hat{F}(\mathbf{k}) \text{TF}(\mathbf{k}, d_{\text{delay}}; w(\theta)) \end{aligned} \quad (7)$$

where $F(\mathbf{k}, d_{\text{delay}})$ is the 2D Fourier spectrum of an image with a specific delay d_{delay} . $\mathbf{k} = (k_x, k_y)$ is the k-space coordinate in the spatial frequency domain. $\hat{F}(\mathbf{k})$ is the Fourier transform of the aberration-free image $\hat{I}(\mathbf{r}')$. From (4), one can express TF as a function of $w(\theta)$. In polar coordinates, it reads (see Appendix B for further details):

$$\text{TF}(k, \theta, d_{\text{delay}}; w(\theta)) = \frac{1}{2} \left(e^{-jk(d_{\text{delay}} - w(\theta))} + e^{jk(d_{\text{delay}} - w(\theta + \pi))} \right), \quad (8)$$

where $j = \sqrt{-1}$ is the imaginary unit. The Fourier domain relationship in Eq. (7) is the key to our APACT algorithm. As shown in Fig. 2(d), (e), and (f), we can decompose $F(\mathbf{k}, d_{\text{delay}})$ into the product of two terms: $\hat{F}(\mathbf{k})$ and TF . The decomposition can be accomplished using the least-square optimization shown below:

$$\underset{w(\theta)}{\text{argmin}} \{ \underset{\hat{F}(\mathbf{k})}{\text{argmin}} \| kF(\mathbf{k}, d_{\text{delay}}) - k\hat{F}(\mathbf{k})\text{TF}(\mathbf{k}, d_{\text{delay}}; w(\theta)) \| \}. \quad (9)$$

A factor $k = \| \mathbf{k} \|$ is introduced because in the Fourier domain the noise level is inversely proportional to k (see Appendix B for further details). This optimization not only extracts the wavefront function but also estimates the Fourier domain aberration-free image $\hat{F}(\mathbf{k})$. An inverse Fourier transform is performed to recover the spatial domain image as shown in Fig. 2(g).

The optimization of Eq. (9) is done by exhaustive search for $w(\theta)$ and a linear least square projection for $\hat{F}(\mathbf{k})$. In AO, the wavefront distortion

function is often decomposed into Zernike modes where higher-order modes can be discarded [35]. In our implementation, the searching of $w(\theta)$ is confined to its 0th and 2nd Fourier series coefficients, which can greatly reduce the computation time. In Appendix C we prove that the 1st order coefficient cannot be extracted, the situation bears a resemblance to the tip and tilt Zernike modes [46] that can only result in a position shift of the image but has no influence on image quality.

2.3. Image stitching and SOS reconstruction

After all the isoplanatic patches are deconvolved (either sequentially or in parallel) following the above procedure, we stitch them together to get the full image. In addition, we can also use the extracted wavefronts to calculate an SOS distribution.

In our simulation, phantom, and *in vivo* experiments, the size of the isoplanatic patch was chosen to be 3.2mm × 3.2mm. To apply Fourier transform, a Gaussian window was multiplied, confining the effective area to a disk with a full width at half maximum of 1.5 mm. The recovered images inherit the Gaussian modulation, as can be seen in Fig. 2(g). These local images are stitched together, with neighboring patches partially overlapped and superimposed, to generate the full image. By design, a 75% overlap between neighboring patches was employed, as shown in Fig. 2(a) by the red and blue dashed boxes. The overall shape, resulting from adding the Gaussian profiles, will become flat. Because the Gaussian window is close to zero on the patch edges, the interpatch transition will be smooth.

To estimate the SOS map, acoustic refraction was neglected, i.e., ultrasound rays do not bend during propagation and the resulting TOF is computed by a straight line integral of the reciprocal of the SOS [25]. We built linear equations on these reciprocals and solved the equations with regularization. A detailed algorithm is provided in Appendix D. We only computed the SOS in the sample/animal body while the SOS of the surrounding water was estimated by measuring the temperature [47].

3. Result

3.1. Numerical simulation

We used k-Wave toolbox [48] to do the simulation in 2D. To approximate the real case with transducer response, we take the derivative of the simulated signals: $S(n, t) = -2 \frac{\partial p(r(n), t)}{\partial t}$. The numerical phantom had an SOS of 1600 m/s with a circular inclusion whose SOS was 1650 m/s, as shown in Fig. 3(e). The SOS of the surrounding water was set to 1500 m/s. We used a vascular mimicking pattern for the PA contrast (Fig. 3(b)).

The results of image reconstruction are shown in Fig. 3. Compared to the severely distorted image shown in Fig. 3(c), which was reconstructed by DAS assuming a constant speed of sound (the SOS was already tuned for best visual effect), APACT corrected the aberrations to yield better image quality (Fig. 3(d)). The image quality is comparable to Fig. 3(b), the best aberration-free image we can get when the SOS is homogenous.

The extracted wavefronts and the SOS reconstruction result are also shown. The wavefront distortions are displayed in polar plots as in Fig. 2(h). In Fig. 3(g), each little ellipse represents a snapshot of the acoustic wavefront outside the phantom emanating from a virtual point source located at the center of the ellipse, while the distortion is exaggerated. The ellipses tend to align their major axes radially because traversing the phantom advances the wavefront due to a higher average SOS.

In places with no or weak PA features, it is not possible to use the algorithm to extract the wavefront due to a lack of “guide stars”. In Fig. 3(g) we also plotted the correct wavefronts (only 0th and 2nd order distortions were extracted and drawn), which were calculated directly from Snell’s law. As shown in Fig. 3(g), in the featureless regions, wavefront estimation is prone to errors. Although noise was absent in the simulation, the energy leakage from nearby patches dominated and generated

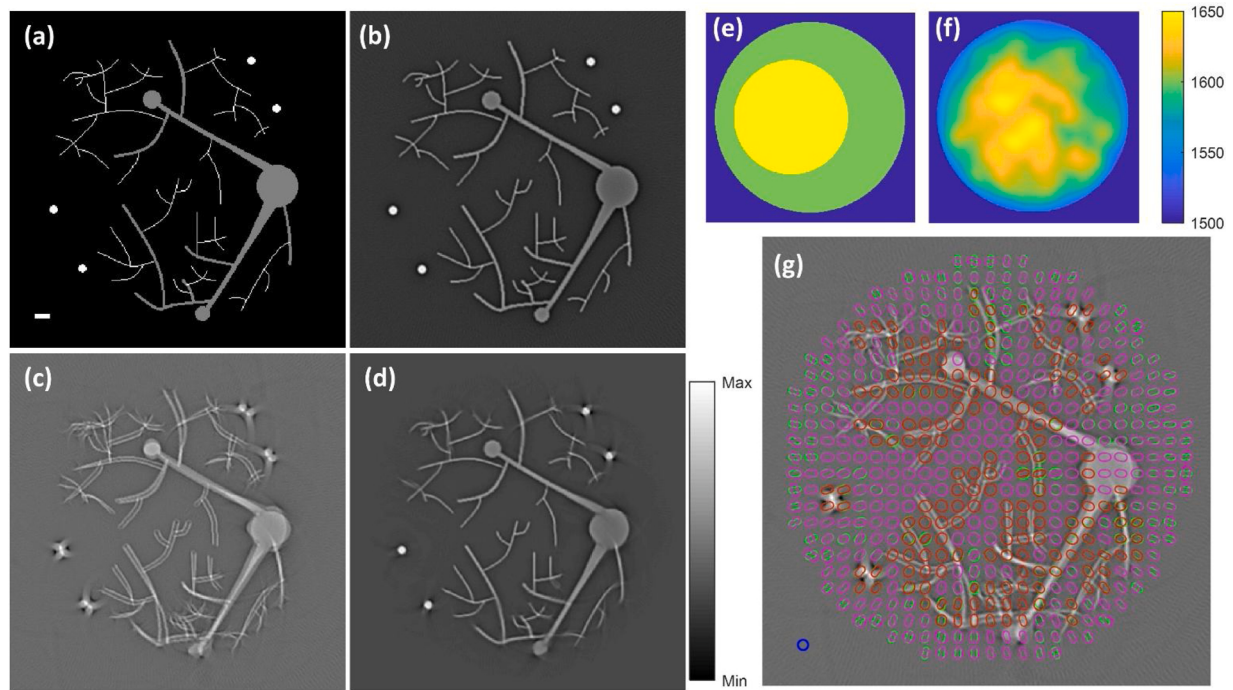


Fig. 3. Numerical simulation results. (a) The gold standard of the IP distribution. Scale bar: 1 mm. (b) Image reconstructed using conventional DAS for an acoustically homogeneous phantom with $SOS = 1500$ m/s. (c) Image reconstructed using conventional DAS for the acoustically inhomogeneous phantom shown in (e) with $SOS = 1520$ m/s. (d) Image reconstructed using APACT. (e) The gold standard of the SOS map. (f) Recovered SOS map. (e) and (f) share the same color bar. (g) The extracted wavefronts are drawn on top of the original image. Red ellipses: estimated wavefronts with a relative fitting error of less than 50%; Purple ellipses: estimated wavefronts with a relative fitting error above 50%. Green ellipses: real wavefronts. Blue circle (bottom left): aberration-free wavefront propagating at 1520 m/s. (For interpretation of the references to colour in this figure legend, the reader is referred to the web version of this article).

errors. Such unfavorable situations can be identified during the fitting process of Eq. (9), where the mismatch between the two terms is noticeably high irrespective of the choice of $w(\theta)$. A “relative error” can be defined as the value of the mismatch normalized by the total energy

of $kF(k, d_{\text{delay}})$. To calculate the SOS map, in the simulation we discarded all the wavefronts whose relative error exceeded 50%, as shown in purple in Fig. 3(g). The result of the SOS distribution reconstruction is shown in Fig. 3(f). Compared to the real SOS distribution shown in Fig. 3

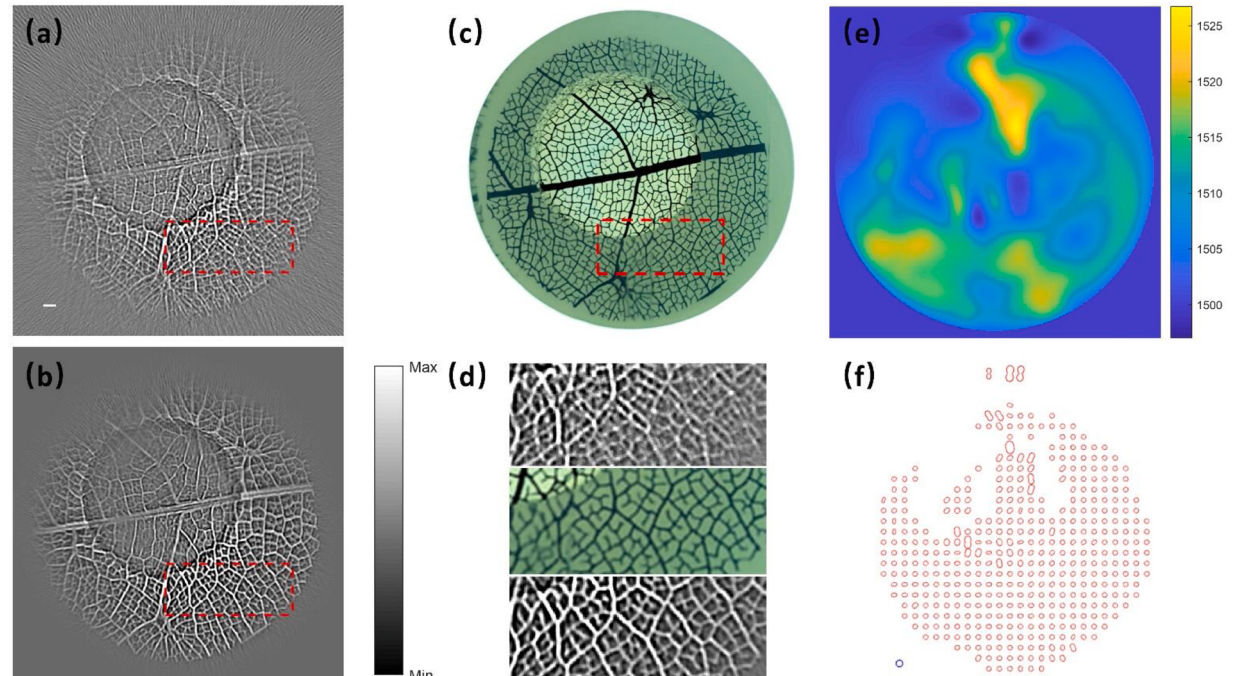


Fig. 4. Phantom imaging results. (a) Image reconstructed using conventional DAS. (b) Image reconstructed using APACT. (c) Photo of the phantom. (d) Top-down: zoomed-in views of the regions highlighted in red dashed boxes in (a), (c), and (b). (e) Recovered SOS map. (f) Red ovals: extracted wavefronts with relative fitting errors below 70%. Blue circle (bottom left): aberration-free wavefront propagating at 1505 m/s. Scale bar: 1 mm. (For interpretation of the references to colour in this figure legend, the reader is referred to the web version of this article).

(e), estimation errors do exist; however, a general similarity is observed.

3.2. Phantom experiment

To verify the performance of APACT, we did a phantom experiment. We used a colored leaf vein as the PA target. A photo of the phantom is shown in Fig. 4(c).

We embedded the leaf in a 2.5 cm diameter agarose cylinder (solution made by mixing 4 g agarose with 100 g water). The dyed leaf vein was embedded into the phantom perpendicular to the height direction. A cylindrical hole running parallel to the phantom was created, which was filled with water during the experiment. Because agarose has a higher SOS than water, this phantom represents a case of very uneven SOS distribution. The water temperature was measured to be 26°C during the experiment.

An image reconstructed using conventional DAS ($SOS = 1505 \text{ m/s}$) is shown in Fig. 4(a). The laser illumination was at 700 nm. Because the phantom was not optically turbid enough, illumination inside the phantom was not uniform, resulting in lower SNR on the upper left corner of the image. In Fig. 4(b) we presented the result of the image reconstructed using APACT. Compared to Fig. 4(a), the image quality is

apparently improved. From the zoomed-in views shown in Fig. 4(d), we can compare the reconstruction results with the real structure of the leaf vein to examine the fidelity of different reconstruction algorithms.

The extracted wavefronts are depicted in Fig. 4(f). In the experiment, due to the existence of noise, we increased the threshold for relative error to 70%, and the survived wavefronts are shown in Fig. 4(f). The missing wavefront plots on the upper-left corner correspond to the region with low SNR.

The reconstruction of the SOS distribution is shown in Fig. 4(e). The regions with higher SOS correlate reasonably well with the solid agar shown in Fig. 4(c). It is worth mentioning that the ellipticity of the ring array, due to manufacturing imperfection, can also contribute to the wavefront function defined in Eq. (3). So to compute the SOS map, $w(\theta)$ should be adjusted to remove this geometrical offset. We measured the geometrical error $w_{GE}(\theta)$ using a PA point source, and subtracted its 0th and 2nd order components from $w(\theta)$ before drawing Fig. 4(f) and computing the SOS distribution. We followed the same procedure in the *in vivo* experiment.

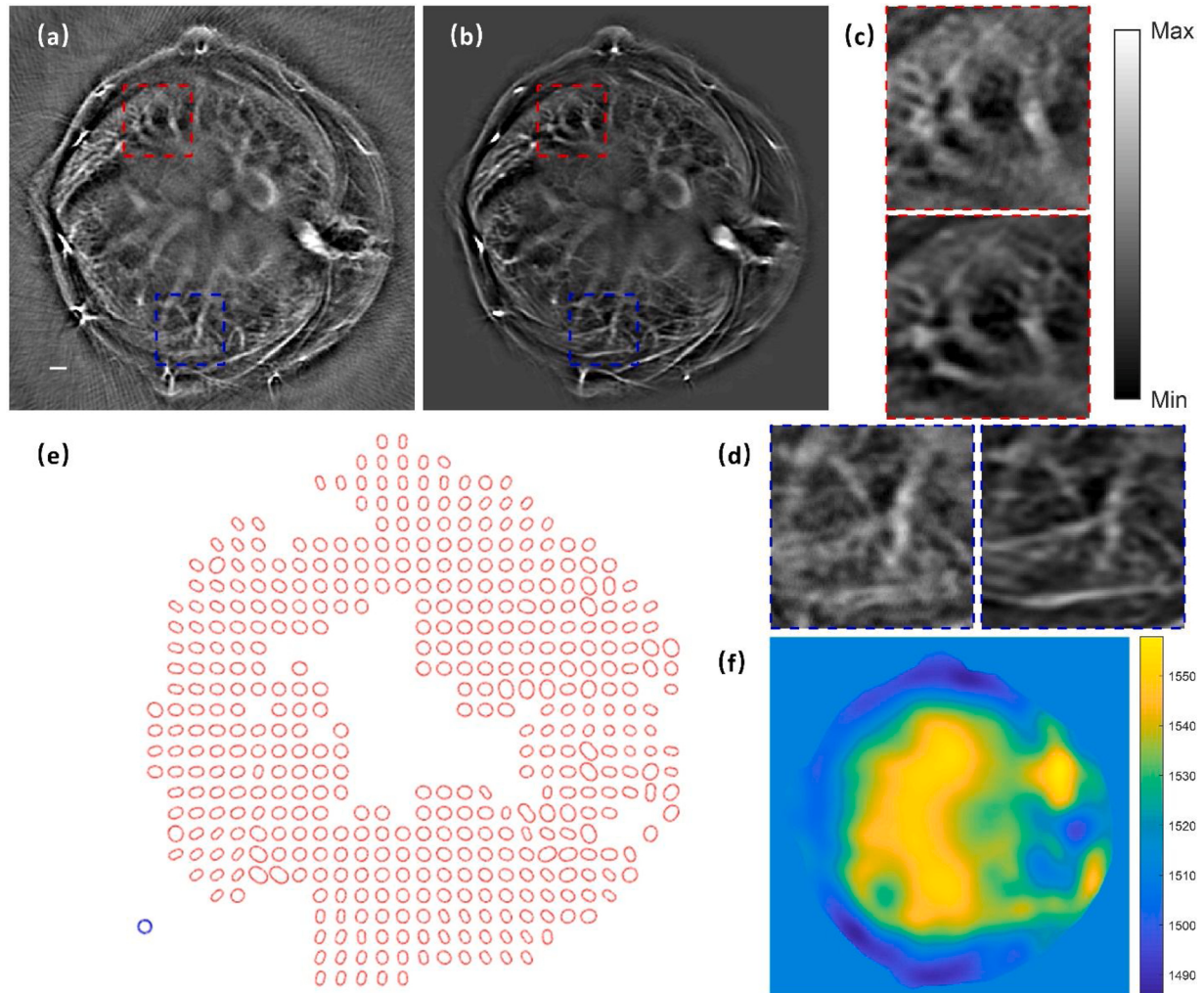


Fig. 5. *In vivo* imaging results. (a) Image reconstructed using conventional DAS. (b) Image reconstructed using APACT. (c, d) The zoomed-in area of (a) and (b) in the red and blue dashed line boxes, respectively. (e) Red ovals: extracted wavefronts with relative fitting errors below 70%. Blue circle (bottom left): aberration-free wavefront propagating at 1515 m/s. (f) Recovered SOS map. Scale bar: 1 mm. (For interpretation of the references to colour in this figure legend, the reader is referred to the web version of this article).

3.3. In vivo experiment

In the *in vivo* experiment, we imaged a nude mouse (8-week-old CrI:NU-Foxn 1^{nu} mouse) in the liver region at 1064 nm. (The same data has been used in another work [14] of our lab.) The water temperature was maintained at 31°C during the experiment. Compared to Fig. 5(a) which was reconstructed using conventional DAS, the APACT reconstruction result shown in Fig. 5(b) shows better quality. For example, the vertical vessels close to the surface of the body are shown as bright spots in Fig. 5(b) but appear to be highly distorted in Fig. 5(a).

Two zoomed-in areas with abundant features of blood vessels are shown in Fig. 5(c) and (d). Without a gold standard, it is difficult to judge which reconstruction outperforms the other. However, the APACT images appear to be superior visually with smoother texture and sharper features, which are hallmarks of better focusing. Similar improvements are prevalent in the entire image.

We also chose to use the wavefronts whose relative fitting error is less than 70% to calculate the SOS map. The wavefront map shown in Fig. 5(e) is physically reasonable because the ovals near the edge tend to align their major axes towards the center, while those close to the center are slightly dilated yet less elongated. This trend can be explained by the higher SOS of the mouse than the surrounding water. The computed SOS distribution is shown in Fig. 5(f), indicating a higher SOS value in some parts of the body, which can be anatomically identified as the liver.

4. Discussion

In this work, we propose and demonstrate a PACT image reconstruction algorithm to remove artifacts caused by non-uniform SOS. Traditional JR methods optimize the SOS distribution together with the PA image iteratively. Without prior knowledge about the SOS distribution, the degrees of freedom of the overall optimization is large. In such cases, the iteration may fall into a local extremum, while the resulting reconstruction is suboptimal. However, our method establishes an entirely new strategy to avoid such a problem. We found that the problem of solving the unknown SOS distribution can be decomposed into independent local wavefront extraction problems. This means the overall image quality does not suffer much from an incorrectly resolved local wavefront.

The estimation accuracy of $w(\theta)$ relies on the sufficiency of the spatial frequency components in all directions in the selected patch. With incomplete frequency components, wavefront estimations are likely to be corrupted. This can be seen in both the simulation and the experimental results. Fortunately, image correction is less affected because the spectrum of the image has little proportion of energy in those unfavorable directions. On the contrary, to compute the SOS map, the set of equations can be underdetermined to begin with, whereas incorrect wavefront estimations simply exacerbate the situation. The regularization we employed in this study assumed that SOS variations are spatially slow, which may not be true in reality. Despite the above difficulties, the major advantage of APACT over JR is that the IP can be recovered reliably if PA features are abundant, and for each recovered patch, the accuracy of the extracted wavefront can be inferred from the fitting error of Eq. (9).

As a newly developed reconstruction algorithm, APACT's capacity is yet to be fully developed. Examining Fig. 3(b) and (d), one can see that the recovered image is smaller as if a scaling factor is applied. This is because the 1st order wavefront distortion cannot be corrected by our algorithm. The resolved image features shift inwards due to the different wavefront distortion in opposing directions. This 1st order distortion can

be calculated using the reconstructed SOS distribution. Also, making use of global information can make the solution more stable. Further restrictions can be imposed on $w(\theta)$ from a global perspective to avoid apparent inconsistency among different patches. To further improve the performance of the algorithm, the frequency domain technique using Eq. (9) can also be modified – blind deconvolution, and prior knowledge about $P_0(r')$ such as nonnegativity [49] can be applied for better accuracy.

Although the focused ring array system was used throughout this study, the method can be extended to other array geometries with modified formulas. In the current system, the out-of-focus signals may contaminate the in-plane ones, making our model inaccurate and adversely affect the overall performance. So we expect even better performance when both PA signal detection and image reconstruction are extended to 3D.

5. Conclusion

Herein we present an image reconstruction algorithm in PACT with adaptive wavefront correction that bears a strong resemblance to AO in optical microscopy. Using the new method, PACT image aberrations induced by SOS heterogeneity can be remedied locally. The wavefront distortion is defined as a perturbation added on the ideal spherical wavefront. We derived that this distortion, which corresponds to a signal arrival time difference, will mathematically determine a distorted point spread function. In an isoplanatic patch where wavefront distortion is almost translational invariant, the distorted image can be regarded as the initial pressure convolved with a distorted PSF. To locally decode the wavefront information, a phase diversity technique is used: A series of local images within an isoplanatic patch is reconstructed, in which various delays are used in the conventional delay-and-sum image reconstruction process. These images originate from the same target but are blurred by different PSFs. From the Fourier transforms of these images, we can extract both the wavefront distortion and the aberration-free image. The patches are then stitched together to form the whole image. Then by solving a set of linear equations, we used the extracted wavefronts to calculate the SOS map. Because the PA image and SOS map are no longer simultaneously reconstructed, our method is more stable and is unlikely to fall into local extrema. We demonstrated the effectiveness of our method using *in silico*, phantom, and *in vivo* experiments. The method is developed in particular for the full ring array system. In the future, it can be further improved and extended to other PACT detection geometry. We also believe that the concept of APACT can benefit other imaging fields that involve wave propagation in heterogeneous media (e.g., optical microscopy and ultrasound imaging), for simultaneous image deblurring and mapping of the wave speed distribution.

Declaration of Competing Interest

The authors declare that they have no known competing financial interests or personal relationships that could have appeared to influence the work reported in this paper.

Acknowledgments

This research was supported by National Natural Science Foundation of China (61735016, 61971265) and Tsinghua University (Seed Foundation of Dept of EE).

Appendix A. Explanations of the mathematical expression for the point spread function

The point spread function (PSF) of a linear imaging system is defined as the image of a point source. Any complex image can be seen as the linear superposition of the PSF at an infinite number of point sources. In our case, it is the reconstructed PACT image when the initial photoacoustic pressure is a Dirac delta function $p(\mathbf{r}, 0) = \delta(\mathbf{r}' - \mathbf{r})$.

The amplitude of the ultrasound pressure originates from this source is inversely proportional to the propagation distance, but the signal detected by the transducers has the same profile, known as the electrical impulse response $h(t)$. The definition of EIR is more rigorously regarded as the sensor's response to a delta excitation $h_0(t)$. However, the impulse generated photoacoustically is the first-order derivative of a delta function, which generates a response $h(t) = \frac{d}{dt}h_0(t)$. As such, in this paper, it is more convenient to use $h(t)$ to refer to the signal generated by a point photoacoustic source, which is then back-projected in the DAS algorithm. In the DAS algorithm, the signal detected by a transducer element is projected to an arc centered at that transducer element. The envelope of the arc is $h(t)$ while the spatial and temporal domains are linked by the speed of sound \hat{v}_s , and the amplitude of the profile decays as $\frac{A}{\|\mathbf{r}' - \mathbf{r}(t)\|}$. Here, we treat the arcs as straight lines. This treatment is valid when we confine the analysis to a small fraction of the back-projected arcs. It is justified by the fact that the majority of the energy of the PSF is localized and the parts of arcs that extend far away from the PSF center are of little significance. There exists leakage of the PSF energy to patches far away, but we just treat that as noise. Because of the signal arriving time changes due to wavefront distortion, each line will be shifted slightly away from the point source position, which is defined as the origin for the vector \mathbf{x} . The equation that describes the lines are $\hat{\mathbf{n}}_i \cdot \mathbf{x} + w(\theta_i, \mathbf{r}') = 0$, where $\hat{\mathbf{n}}_i \equiv \frac{\mathbf{r}' - \mathbf{r}(i)}{\|\mathbf{r}' - \mathbf{r}(i)\|}$ is the normal vector of the lines which is also the direction pointing at the source from the i th transducer position. $\hat{\mathbf{n}}_i$ is also the shifting direction or the backpropagation direction of this signal. $w(\theta_i, \mathbf{r}')$ is the shift amount. We sum all the ridge-like functions together to finally reach the formula of PSF in Eq. (4).

Appendix B. Derivation of the transfer function

Denote $H(\omega)$ as the Fourier transform of $h(t)$, where ω is the angular frequency. In our derivations, $H(\omega)$ is assumed to be real, which means there is no frequency-dependent delay in the system. In a real system, this may not be true. But it is easy to do a phase adjustment for all the channels digitally using FFT to correct the dispersion. Additionally, because $h(t)$ is real, we have $H(\omega) = H(-\omega)$.

We now perform 2D Fourier transform to Eq. (4). Mathematically, inside the summation, the Fourier transform can be performed firstly along the direction $\hat{\mathbf{n}}_i$, and then along its perpendicular direction $\hat{\mathbf{t}}_i$ ($\hat{\mathbf{t}}_i \perp \hat{\mathbf{n}}_i$). Here $x_n = \hat{\mathbf{n}}_i \cdot \mathbf{x}$ and $x_\tau = \hat{\mathbf{t}}_i \cdot \mathbf{x}$ are the components along these two directions. In the spatial frequency domain, we also decompose the \mathbf{k} vector along the orthogonal directions $k_n = \hat{\mathbf{n}}_i \cdot \mathbf{k}$ and $k_\tau = \hat{\mathbf{t}}_i \cdot \mathbf{k}$.

$$\begin{aligned} \mathcal{F}\left\{PSF(\mathbf{x}; w(\theta))\right\} &= \mathcal{F}\left\{\sum_{i=1}^N \frac{A}{\|\mathbf{r}' - \mathbf{r}(i)\|} h\left(\frac{\hat{\mathbf{n}}_i \cdot \mathbf{x} + w(\theta_i)}{\hat{v}_s}\right)\right\} \\ &= \sum_{i=1}^N \frac{A}{\|\mathbf{r}' - \mathbf{r}(i)\|} \iint h\left(\frac{x_n + w(\theta_i)}{\hat{v}_s}\right) e^{-jx_n k_n} e^{-jx_\tau k_\tau} dx_n dx_\tau \\ &= \sum_{i=1}^N \frac{A \hat{v}_s}{\|\mathbf{r}' - \mathbf{r}(i)\|} \int H(k_n \hat{v}_s) e^{jk_n w(\theta_i)} e^{-jx_\tau k_\tau} dx_\tau \\ &= \sum_{i=1}^N \frac{A \hat{v}_s}{\|\mathbf{r}' - \mathbf{r}(i)\|} H(k_n \hat{v}_s) e^{jk_n w(\theta_i)} 2\pi \delta(k_\tau) \\ &= \sum_{i=1}^N \frac{A \hat{v}_s}{\|\mathbf{r}' - \mathbf{r}(i)\|} H(\hat{\mathbf{n}}_i \cdot \mathbf{k} \hat{v}_s) e^{j\hat{\mathbf{n}}_i \cdot \mathbf{k} w(\theta_i)} 2\pi \delta(\hat{\mathbf{t}}_i \cdot \mathbf{k}) \end{aligned} \quad (\text{B.1})$$

This expression derived above has a stellate structure consisting of many Dirac delta functions $\delta(\hat{\mathbf{t}}_i \cdot \mathbf{k})$. That is because the back projection arcs are idealized to infinitely-long straight lines in Eq. (4), and the portions far away should be discarded. Equivalent to the truncation of the lines in the spatial domain (i.e. multiplying a window, corresponding to a convolution in the spatial frequency domain), we can implement a smooth operation to those delta functions by calculating the average amplitude over small areas. In our system, the transducers are densely arranged, so we calculate the average in the polar coordinate region $[\theta, \theta + d\theta] \times [k, k + dk]$ to be $\overline{\mathcal{F}\{PSF(\mathbf{x})\}}$. The transducers whose corresponding delta functions fall into the region are those whose $\hat{\mathbf{n}}_i$ are directed close to θ or $\theta + \pi$, and consequently, their total number can be estimated as $N \frac{L(\theta) d\theta}{2\pi R}$ or $N \frac{L(\theta + \pi) d\theta}{2\pi R}$, respectively, where R is the transducer array radius. Where $L(\theta)$ is the distance between \mathbf{r}' and the transducer whose $\hat{\mathbf{n}}_i$ is in the direction of θ . As a result,

$$\begin{aligned} \overline{\mathcal{F}\{PSF(\mathbf{x}; w(\theta))\}} k dk d\theta &= \left[N \frac{L(\theta) d\theta}{2\pi R} \right] \frac{2\pi dk}{L(\theta)} A \hat{v}_s \cdot H(k \hat{v}_s) e^{jk w(\theta)} \\ &\quad + \left[N \frac{L(\theta + \pi) d\theta}{2\pi R} \right] \frac{2\pi dk}{L(\theta + \pi)} A \hat{v}_s \cdot H(-k \hat{v}_s) e^{-jk w(\theta + \pi)}. \end{aligned} \quad (\text{B.2})$$

After further simplification, Eq. (B.2) can be expressed as

$$\overline{\mathcal{F}\{PSF(\mathbf{x}; w(\theta))\}} k = \frac{N A \hat{v}_s}{R} H(k \hat{v}_s) (e^{jk w(\theta)} + e^{-jk w(\theta + \pi)}). \quad (\text{B.3})$$

It is important to realize that if white random noise appears in the time domain signal, it will be added onto $H(k \hat{v}_s)$. Then, in the image Fourier domain, the noise level is inversely proportional to $k = \|\mathbf{k}\|$.

The transfer function is the ratio between the Fourier transform of the distorted PSF and the ideal one, as shown below:

$$\begin{aligned} \text{TF}(k, \theta, d_{\text{delay}}; w(\theta)) &= \frac{\overline{\mathcal{F}\{PSF(\mathbf{x}; w(\theta) - d_{\text{delay}})\}}}{\overline{\mathcal{F}\{PSF(\mathbf{x}; 0)\}}} \\ &= \frac{1}{2} (e^{-jk(d_{\text{delay}} - w(\theta))} + e^{jk(d_{\text{delay}} - w(\theta + \pi))}) \end{aligned} \quad (\text{B.4})$$

Appendix C. The Fourier series expansion of the wavefront function

The natural periodic boundary condition of $w(\theta)$ makes it easy for us to consider the harmonic expansion of the function:

$$w(\theta) = C_0 + C_1 \cos(\theta - \phi_1) + C_2 \cos(2\theta - \phi_2) + \dots \quad (\text{C.1})$$

After propagation in the water, the wavefront will become smooth which means the high order distortion is very low. A problem is that the 1st order distortion: $C_1 \cos(\theta - \phi_1)$ can not be extracted and corrected using our method. This is because

$$\widehat{F}(\mathbf{k}) TF(\mathbf{k}, d_{\text{delay}}; w(\theta) - C_1 \cos(\theta - \phi_1)) = \widehat{F}(\mathbf{k}) e^{-jkC_1 \cos(\theta - \phi_1)} TF(\mathbf{k}, d_{\text{delay}}; w(\theta)) \quad (\text{C.2})$$

This means the least square fitting error of Eq. (9) will not change if we subtract the 1st order component from $w(\theta)$, and it will only lead to a different estimated $\widehat{F}(\mathbf{k})$. This is very much like the tip-and-tilt Zernike mode in AO. Because in the space domain, the 1st order distortion will cause the PSF to shift C_1 in the direction of ϕ_1 . As shown in the expression below:

$$PSF(\mathbf{x}; w(\theta) - C_1 \cos(\theta - \phi_1)) = \sum_{i=1}^N \frac{A}{\|\mathbf{r}' - \mathbf{r}(i)\|} h\left(\frac{\widehat{\mathbf{n}}_i \cdot \mathbf{x} + w(\theta_i) - C_1 \cos(\theta_i - \phi_1)}{\widehat{v}_s}\right) \quad (\text{C.3})$$

On the other hand, if the PSF is translated by a vector \mathbf{c} ,

$$PSF(\mathbf{x} - \mathbf{c}; w(\theta)) = \sum_{i=1}^N \frac{A}{\|\mathbf{r}' - \mathbf{r}(i)\|} h\left(\frac{\widehat{\mathbf{n}}_i \cdot \mathbf{x} - \widehat{\mathbf{n}}_i \cdot \mathbf{c} + w(\theta_i)}{\widehat{v}_s}\right) \quad (\text{C.4})$$

We only have to let the direction of \mathbf{c} be ϕ_1 and its length equal to C_1 to make the two expressions equal. This shift can also be seen in Eq. (C.2). The factor $e^{-jkC_1 \cos(\theta - \phi_1)}$ is in fact a tilt factor indicating that the estimation of the distortion-free image is also a shifted version without image quality degradation, so we don't care about the 1st order distortion. The above analysis justifies the implementation of our wavefront extraction algorithm, which confines the searching for $w(\theta)$ to the 0th and 2nd Fourier coefficients.

Appendix D. SOS reconstruction algorithm

It is a good approximation [7] that the TOF can be expressed as

$$TOF(\mathbf{r}', \mathbf{r}) = \int_{\text{line segment } \mathbf{r}' - \mathbf{r}} \frac{1}{v_s(\mathbf{q})} dl \quad (\text{D.1})$$

where $v_s(\mathbf{q})$ is the spatially varying SOS distribution. Using this model we can build linear equations on $\frac{1}{v_s(\mathbf{q})}$ when knowing a number of TOFs defined on pairs of points. But as we have proved in the last section, we only have access to the 0th and 2nd order distortion. The orthogonality of the Fourier bases leads to the following relations:

$$\int_0^{2\pi} w(\theta, \mathbf{r}') \frac{1}{2\pi} d\theta = C_0 \quad (\text{D.2})$$

$$\int_0^{2\pi} w(\theta, \mathbf{r}') \frac{\cos(2\theta)}{\pi} d\theta = C_2 \cos(\phi_2) \quad (\text{D.3})$$

$$\int_0^{2\pi} w(\theta, \mathbf{r}') \frac{\sin(2\theta)}{\pi} d\theta = C_2 \sin(\phi_2) \quad (\text{D.4})$$

For each isoplanatic patch, the 3 coefficients will lead to 3 equations on $\frac{1}{v_s(\mathbf{q})}$. Let's take the second one Eq. (D.3) as an example, while the others are the same except that the $\frac{\cos(2\theta)}{\pi}$ term is replaced.

Recall the definition $w(\theta, \mathbf{r}') = \|\mathbf{r}' - \mathbf{r}\| - TOF(\mathbf{r}', \mathbf{r}) \widehat{v}_s$. We use the straight-line integration:

$$\int_0^{2\pi} w(\theta, \mathbf{r}') \frac{\cos(2\theta)}{\pi} d\theta = \int_0^{2\pi} \left(\|\mathbf{r}' - \mathbf{r}\| - \int_{\text{line segment } \mathbf{r}' - \mathbf{r}} \frac{1}{v_s(\mathbf{q})} \widehat{v}_s dl \right) \frac{\cos(2\theta)}{\pi} d\theta, \quad (\text{D.5})$$

where \mathbf{q} is the integration variable. Note that $\|\mathbf{r}' - \mathbf{r}\| = \int_{\text{line segment } \mathbf{r}' - \mathbf{r}} dl$, regarding \mathbf{q} as integration variable and θ can also be seen as the direction pointing from \mathbf{q} to \mathbf{r}' . The differential term can be transformed to the area element: $dld\theta = \frac{dA}{\|\mathbf{r}' - \mathbf{q}\|}$, where $dA = dq_x dq_y$. We can derive:

$$\int_0^{2\pi} w(\theta, \mathbf{r}') \frac{\cos(2\theta)}{\pi} d\theta = \iint_{\text{inside ring array}} \left(1 - \frac{\widehat{v}_s}{v_s(\mathbf{q})} \right) \frac{\cos(2\theta)}{\pi} \frac{dA}{\|\mathbf{r}' - \mathbf{q}\|} \quad (\text{D.6})$$

We know that outside the mouse body, the coupling media is water whose sound speed is known according to the temperature measured in the experiment denoted as v_w . The equation can now be expressed as

$$\begin{aligned} \int_0^{2\pi} w(\theta, \mathbf{r}') \frac{\cos(2\theta)}{\pi} d\theta &= \iint_{\text{inside ring array}} \left(1 - \frac{\widehat{v}_s}{v_w} \right) \frac{\cos(2\theta)}{\pi} \frac{dA}{\|\mathbf{r}' - \mathbf{q}\|} \\ &\quad + \iint_{\text{inside animal body}} \left(\frac{\widehat{v}_s}{v_w} - \frac{\widehat{v}_s}{v_s(\mathbf{q})} \right) \frac{\cos(2\theta)}{\pi} \frac{dA}{\|\mathbf{r}' - \mathbf{q}\|}. \end{aligned} \quad (\text{D.7})$$

Here we put the unknown values on the left side

$$\iint_{\text{inside animal body}} \left(\frac{\hat{v}_s}{v_w} - \frac{\hat{v}_s}{v_s(\mathbf{q})} \right) \frac{\cos(2\theta)}{\pi} \frac{dA}{\|\mathbf{r}' - \mathbf{q}\|} = C_2 \cos(\phi_2) - \iint_{\text{inside ring array}} \left(1 - \frac{\hat{v}_s}{v_w} \right) \frac{\cos(2\theta)}{\pi} \frac{dA}{\|\mathbf{r}' - \mathbf{q}\|}, \quad (\text{D.8})$$

where $\left(\frac{\hat{v}_s}{v_w} - \frac{\hat{v}_s}{v_s(\mathbf{q})} \right)$ is unknown. To discretize the above formula into linear equations, we need to pixelate the SOS distribution. The matrix elements in the row of this equation, corresponding to the coefficient of a pixel, is $\iint_{\text{inside pixel}} \frac{\cos(2\theta)}{\pi} \frac{dA}{\|\mathbf{r}' - \mathbf{r}\|}$. All the function integrations are calculated using MATLAB. We denote the matrix as A , the unknown $\left(\frac{\hat{v}_s}{v_w} - \frac{\hat{v}_s}{v_s(\mathbf{q})} \right)$ value of the pixels as vector θ , and the right side of the equations as X . It is obvious that the number of equations which is 3 times the isoplanar patches number is much smaller than the number of unknowns. Note that we have discussed in the paper that we discard the equations whose corresponding least-square fitting error is too large. So the real number of the equations can be even less. We choose to solve the matrix equation using the Linear Minimum Mean Square Error (Linear MMSE) estimation [50]. The statistic model is that we have a zero-mean independent noise vector n .

$$A\theta + n = X \quad (\text{D.9})$$

We assume that the expectation of θ and n are both zero. $C_{\theta\theta}$ is the autocorrelation matrix of θ . We let the correlation between two pixels be inversely proportional to the exponential of the squared distance between the two pixels, which physically means that the SOS variation is spatially slow. C_{nn} , the noise vector's autocorrelation is assumed to be a diagonal matrix and the variances are proportional to the least square fitting error of Eq. (9). The relative scale between $C_{\theta\theta}$ and C_{nn} , which indicates an SNR estimation on our wavefront extraction results, is tuned in the experiments to get a reasonable result.

We can derive the autocorrelation of X :

$$C_{XX} = AC_{\theta\theta}A^T + C_{nn} \quad (\text{D.10})$$

The cross-correlation matrix of X and θ is

$$C_{\theta X} = C_{\theta\theta}A^T. \quad (\text{D.11})$$

And we can finally reach the LMMSE:

$$\hat{\theta} = E(\theta) + C_{\theta X}C_{XX}^{-1}(X - E(X)) = C_{\theta\theta}A^T(AC_{\theta\theta}A^T + C_{nn})^{-1}X. \quad (\text{D.12})$$

After $\left(\frac{\hat{v}_s}{v_w} - \frac{\hat{v}_s}{v_s(\mathbf{q})} \right)$ it is solved, we can get the sound speed value $v_s(\mathbf{q})$ at each pixel using a simple algebraic conversion.

References

- [1] M. Xu, L.V. Wang, Photoacoustic imaging in biomedicine, Rev. Sci. Instrum. 77 (4) (2006), 041101, <https://doi.org/10.1063/1.2195024>.
- [2] L.V. Wang, S. Hu, Photoacoustic tomography: in vivo imaging from organelles to organs, Science 335 (6075) (2012) 1458–1462, <https://doi.org/10.1126/science.1216210>.
- [3] J. Xia, C. Huang, K. Maslov, M.A. Anastasio, L.V. Wang, Enhancement of photoacoustic tomography by ultrasonic computed tomography based on optical excitation of elements of a full-ring transducer array, Opt. Lett. 38 (16) (2013) 3140–3143, <https://doi.org/10.1364/OL.38.003140>.
- [4] C. Huang, L. Nie, R.W. Schoonover, Z. Guo, C.O. Schirra, M.A. Anastasio, L. V. Wang, Aberration correction for transcranial photoacoustic tomography of primates employing adjoint image data, J. Biomed. Opt. 17 (6) (2012), 066016, <https://doi.org/10.1117/1.JBO.17.6.066016>.
- [5] E. Mercep, J.L. Herráiz, X.L. Deanben, D. Razansky, Transmission-reflection optoacoustic ultrasound (tropus) computed tomography of small animals, Light-Sci. Appl. 8 (1) (2019) 18, <https://doi.org/10.1038/s41377-019-0130-5>.
- [6] J. Jose, R.G. Willemink, W. Steenbergen, C.H. Slump, T.G. van Leeuwen, S. Manohar, Speed-of-sound compensated photoacoustic tomography for accurate imaging, Med. Phys. 39 (12) (2012) 7262–7271, <https://doi.org/10.1118/1.4764911>.
- [7] T. Wang, W. Liu, C. Tian, Combating acoustic heterogeneity in photoacoustic computed tomography: a review, J. Innov. Opt. Health Sci. (2020), 2030007, <https://doi.org/10.1142/S1793545820300074>.
- [8] H. Jiang, Z. Yuan, X. Gu, Spatially varying optical and acoustic property reconstruction using finite-element-based photoacoustic tomography, J. Opt. Soc. Am. A-Opt. Image Sci. Vis. 23 (4) (2006) 878–888, <https://doi.org/10.1364/josaa.23.000878>.
- [9] Z. Yuan, Q. Zhang, H. Jiang, Simultaneous reconstruction of acoustic and optical properties of heterogeneous media by quantitative photoacoustic tomography, Opt. Express 14 (15) (2006) 6749–6754, <https://doi.org/10.1364/OE.14.006749>.
- [10] Z. Yuan, H. Jiang, Simultaneous recovery of tissue physiological and acoustic properties and the criteria for wavelength selection in multispectral photoacoustic tomography, Opt. Lett. 34 (11) (2009) 1714–1716, <https://doi.org/10.1364/OL.34.001714>.
- [11] J. Zhang, K. Wang, Y. Yang, M.A. Anastasio, Simultaneous reconstruction of speed-of-sound and optical absorption properties in photoacoustic tomography via a time-domain iterative algorithm, in: International Society for Optics and PhotonicsPhotons Plus Ultrasound: Imaging and Sensing 2008: The Ninth Conference on Biomedical Thermoacoustics, Optoacoustics, and Acousto-Optics, Vol. 6856, 2008, p. 68561F, <https://doi.org/10.1117/12.764171>.
- [12] C. Huang, K. Wang, R.W. Schoonover, L.V. Wang, M.A. Anastasio, Joint reconstruction of absorbed optical energy density and sound speed distributions in photoacoustic computed tomography: a numerical investigation, IEEE Trans. Comput. Imaging 2 (2) (2016) 136–149, <https://doi.org/10.1109/TCI.2016.2523427>.
- [13] T.P. Matthews, J. Poudel, L. Li, L.V. Wang, M.A. Anastasio, Parameterized joint reconstruction of the initial pressure and sound speed distributions for photoacoustic computed tomography, SIAM J. Imaging Sci. 11 (2) (2018) 1560–1588, <https://doi.org/10.1137/17M1153649>.
- [14] C. Cai, X. Wang, K. Si, J. Qian, J. Luo, C. Ma, Feature coupling photoacoustic computed tomography for joint reconstruction of initial pressure and sound speed in vivo, Biomed. Opt. Express 10 (7) (2019) 3447–3462, <https://doi.org/10.1364/BOE.10.003447>.
- [15] J. Zhang, M.A. Anastasio, Reconstruction of speed-of-sound and electromagnetic absorption distributions in photoacoustic tomography, in: International Society for Optics and PhotonicsPhotons Plus Ultrasound: Imaging and Sensing 2006: The Seventh Conference on Biomedical Thermoacoustics, Optoacoustics, and Acousto-Optics, Vol. 6086, 2006, p. 608619, <https://doi.org/10.1117/12.647665>.
- [16] C. Zhang, Y. Wang, A reconstruction algorithm for thermoacoustic tomography with compensation for acoustic speed heterogeneity, Phys. Med. Biol. 53 (18) (2008) 4971, <https://doi.org/10.1088/0031-9155/53/18/008>.
- [17] H. Shan, G. Wang, Y. Yang, Simultaneous reconstruction of the initial pressure and sound speed in photoacoustic tomography using a deeplearning approach, in: Novel Optical Systems, Methods, and Applications XXII, Vol. 11105, International Society for Optics and Photonics, 2019, p. 1110504, <https://doi.org/10.1117/12.2529984>.
- [18] P. Stefanov, G. Uhlmann, Instability of the linearized problem in multiwave tomography of recovery both the source and the speed, Inverse Probl. Imaging 7 (4) (2013) 1367–1377, <https://doi.org/10.3934/ipi.2013.7.1367>.
- [19] H. Liu, G. Uhlmann, Determining both sound speed and internal source in thermo- and photo-acoustic tomography, Inverse Probl. 31 (10) (2015), 105005, <https://doi.org/10.1088/0266-5611/31/10/105005>.
- [20] C. Knox, A. Moradifam, Determining both the source of a wave and its speed in a medium from boundary measurements, Inverse Probl. (2019), <https://doi.org/10.1088/1361-6420/ab53fc>.
- [21] L. Li, L. Zhu, C. Ma, L. Lin, J. Yao, L. Wang, K. Maslov, R. Zhang, W. Chen, J. Shi, L. V. Wang, Single-impulse panoramic photoacoustic computed tomography of small-animal whole-body dynamics at high spatiotemporal resolution, Nat. Biomed. Eng. 1 (5) (2017) 0071, <https://doi.org/10.1038/s41551-017-0071>.
- [22] M. Xu, L.V. Wang, Universal back-projection algorithm for photoacoustic computed tomography, Phys. Rev. E 71 (1) (2005), 016706, <https://doi.org/10.1103/PhysRevE.71.016706>.

- [23] L.V. Wang, Multiscale photoacoustic microscopy and computed tomography, *Nat. Photonics* 3 (9) (2009) 503, <https://doi.org/10.1038/nphoton.2009.157>.
- [24] M.J. Booth, Adaptive optics in microscopy, *Philos. Trans. Math. Phys. Eng. Sci.* 365 (1861) (2007) 2829–2843, <https://doi.org/10.1098/rsta.2007.0013>.
- [25] Y. Xu, L.V. Wang, Effects of acoustic heterogeneity in breast thermoacoustic tomography, *IEEE Trans. Ultrason. Ferroelectr. Freq. Control* 50 (9) (2003) 1134–1146, <https://doi.org/10.1117/12.477784>.
- [26] J.-W. Cha, J. Ballesta, P.T. So, Shack-hartmann wavefront-sensor-based adaptive optics system for multiphoton microscopy, *J. Biomed. Opt.* 15 (4) (2010), 046022, <https://doi.org/10.1117/1.3475954>.
- [27] R. Aviles-Espinosa, J. Andilla, R. Porcar-Guezanec, O.E. Olarte, M. Nieto, X. Levecq, D. Artigas, P. Loza-Alvarez, Measurement and correction of in vivo sample aberrations employing a nonlinear guide-star in two-photon excited fluorescence microscopy, *Biomed. Opt. Express* 2 (11) (2011) 3135–3149, <https://doi.org/10.1364/BOE.2.003135>.
- [28] X. Tao, B. Fernandez, O. Azucena, M. Fu, D. Garcia, Y. Zuo, D.C. Chen, J. Kubby, Adaptive optics confocal microscopy using direct wavefront sensing, *Opt. Lett.* 36 (7) (2011) 1062–1064, <https://doi.org/10.1364/OL.36.001062>.
- [29] S.A. Rahman, M.J. Booth, Direct wavefront sensing in adaptive optical microscopy using backscattered light, *Appl. Optics* 52 (22) (2013) 5523–5532, <https://doi.org/10.1364/AO.52.005523>.
- [30] O. Azucena, J. Crest, S. Kotadia, W. Sullivan, X. Tao, M. Reinig, D. Gavel, S. Olivier, J. Kubby, Adaptive optics wide-field microscopy using direct wavefront sensing, *Opt. Lett.* 36 (6) (2011) 825–827, <https://doi.org/10.1364/OL.36.000825>.
- [31] X. Tao, J. Crest, S. Kotadia, O. Azucena, D.C. Chen, W. Sullivan, J. Kubby, Live imaging using adaptive optics with fluorescent protein guidestars, *Opt. Express* 20 (14) (2012) 15969–15982, <https://doi.org/10.1364/OE.20.015969>.
- [32] S. Tuohy, A.G. Podoleanu, Depth-resolved wavefront aberrations using a coherence-gated shack-hartmann wavefront sensor, *Opt. Express* 18 (4) (2010) 3458–3476, <https://doi.org/10.1364/OE.18.003458>.
- [33] K. Wang, W. Sun, C.T. Richie, B.K. Harvey, E. Betzig, N. Ji, Direct wavefront sensing for high-resolution in vivo imaging in scattering tissue, *Nat. Commun.* 6 (1) (2015) 1–6, <https://doi.org/10.1038/ncomms8276>.
- [34] O. Albert, L. Sherman, G. Mourou, T.B. Norris, G. Vdovin, Smart microscope: an adaptive optics learning system for aberration correction in multiphoton confocal microscopy, *Opt. Lett.* 25 (1) (2000) 52–54, <https://doi.org/10.1364/OL.25.000052>.
- [35] M.J. Booth, M.A. Neil, R. Juškaitis, T. Wilson, Adaptive aberration correction in a confocal microscope, *Proc. Natl. Acad. Sci. U.S.A.* 99 (9) (2002) 5788–5792, <https://doi.org/10.1073/pnas.082544799>.
- [36] C. Bourgenot, C.D. Saunter, J.M. Taylor, J.M. Girkin, G.D. Love, 3d adaptive optics in a light sheet microscope, *Opt. Express* 20 (12) (2012) 13252–13261, <https://doi.org/10.1364/OE.20.013252>.
- [37] D. Débarre, M.J. Booth, T. Wilson, Image based adaptive optics through optimisation of low spatial frequencies, *Opt. Express* 15 (13) (2007) 8176–8190, <https://doi.org/10.1364/OE.15.008176>.
- [38] N. Ji, D.E. Milkie, E. Betzig, Adaptive optics via pupil segmentation for high-resolution imaging in biological tissues, *Nat. Methods* 7 (2) (2010) 141–147, <https://doi.org/10.1038/nmeth.1411>.
- [39] D.E. Milkie, E. Betzig, N. Ji, Pupil-segmentation-based adaptive optical microscopy with full-pupil illumination, *Opt. Lett.* 36 (21) (2011) 4206–4208, <https://doi.org/10.1364/OL.36.004206>.
- [40] J. Scrimgeour, J.E. Curtis, Aberration correction in wide-field fluorescence microscopy by segmented-pupil image interferometry, *Opt. Express* 20 (13) (2012) 14534–14541, <https://doi.org/10.1364/OE.20.014534>.
- [41] D. Burke, B. Patton, F. Huang, J. Bewersdorf, M.J. Booth, Adaptive optics correction of specimen-induced aberrations in single-molecule switching microscopy, *Optica* 2 (2) (2015) 177–185, <https://doi.org/10.1364/OPTICA.2.000177>.
- [42] N. Ji, Adaptive optical fluorescence microscopy, *Nat. Methods* 14 (4) (2017) 374, <https://doi.org/10.1038/nmeth.4218>.
- [43] M.J. Booth, Adaptive optical microscopy: the ongoing quest for a perfect image, *Light-Sci. Appl.* 3 (4) (2014) e165, <https://doi.org/10.1038/lsa.2014.46>.
- [44] R.A. Gonsalves, Phase retrieval and diversity in adaptive optics, *Opt. Eng.* 21 (5) (1982) 829–832, <https://doi.org/10.1117/12.7972989>.
- [45] B.E. Treeby, T. Varslot, E.Z. Zhang, J. Laufer, P.C. Beard, Automatic sound speed selection in photoacoustic image reconstruction using an autofocus approach, *J. Biomed. Opt.* 16 (9) (2011), 090501, <https://doi.org/10.1117/1.3619139>.
- [46] A. Thayil, M.J. Booth, Self calibration of sensorless adaptive optical microscopes, *J. Eur. Opt. Soc.-Rapid Publ.* 6 (2011) 16, <https://doi.org/10.2971/jeos.2011.11045>.
- [47] W. Marczak, Water as a standard in the measurements of speed of sound in liquids, *J. Acoust. Soc. Am.* 102 (5) (1997) 2776–2779, <https://doi.org/10.1121/1.420332>.
- [48] B.E. Treeby, B.T. Cox, k-wave: Matlab toolbox for the simulation and reconstruction of photoacoustic wave fields, *J. Biomed. Opt.* 15 (2) (2010), 021314, <https://doi.org/10.1117/1.3360308>.
- [49] D. Kundur, D. Hatzinakos, Blind image deconvolution, *IEEE Signal Process. Mag.* 13 (May (3)) (1996) 43–64, <https://doi.org/10.1109/79.489268>.
- [50] S.M. Kay, *Fundamentals of Statistical Signal Processing*, Prentice Hall PTR, 1993.



Manxiu Cui graduated in 2020 from the Department of Electronic Engineering, Tsinghua University. He is currently working as a research assistant in Biophotonics Laboratory, Tsinghua University. In 2021, he will become a graduate student working in Caltech Optical Imaging Laboratory at California Institute of Technology. His research interest is photoacoustic imaging and other optical imaging modalities. His goal is to push the boundaries of the resolution, depth, and fidelity of biomedical imaging techniques.



Hongzhi Zuo graduated from the School of Optics and Photonics, Beijing Institute of technology in 2019. He is now studying for a doctorate in Biophotonics Laboratory, Department of electronic engineering, Tsinghua University. His research focuses on solving the problems of imperfect reconstruction and spectral coloring in multispectral photoacoustic imaging, improving the quantitative imaging ability and functional imaging ability of the existing photoacoustic system.



Xuanhao Wang graduated from the School of Optics and Photonics, Beijing Institute of technology in 2017 who is studying for a doctorate in Biophotonics Laboratory, Department of electronic engineering, Tsinghua University at present. The research focuses on developing advanced photoacoustic computed tomography systems with pathbreaking applications of biological problems.



Kexin Deng graduated from Tsinghua University in 2017. From 2017 to now she works as a Ph.D. student in the Fluorescence Science Laboratory in the medical school of Tsinghua University. Her research interest is linked with the reconstruction problem in photoacoustic imaging and breast tumor screening. She published 2 conference abstracts.



Jianwen Luo is an Associate Professor in the Department of Biomedical Engineering, Tsinghua University, Beijing, China. He has authored or coauthored over 150 articles in international journals and 70 conference proceedings articles. His research interests include ultrasound imaging, fluorescence imaging, and photoacoustic imaging. He serves as an Associate Editor for the IEEE Transactions on Ultrasonics, Ferroelectrics, and Frequency Control, an Advisory Editorial Board Member for the Journal of Ultrasound in Medicine, a Technical Committee Member for the IEEE Engineering in Medicine and Biology Society (EMBS) on Biomedical Imaging and Image Processing (BIP), and a Technical Program Committee Member for the IEEE International Ultrasonics Symposium (IUS).



Cheng Ma received his B.S. degree in Electronic Engineering from Tsinghua University, Beijing, China in 2004. He obtained his Ph. D. degree in Electrical Engineering from Virginia Tech, Blacksburg, Virginia in 2012. From 2012–2016, he was a postdoctoral research associate in the Department of Biomedical Engineering at Washington University in St Louis, St. Louis, Missouri. From May 2016 to present, Cheng Ma is an assistant professor in the Department of Electronic Engineering at Tsinghua University. Until 2020, he has published more than 30 journal papers. His research interests include biophotonic imaging and sensing, in particular photoacoustic imaging and wavefront shaping.